

# Linking microstructure and processing defects to mechanical properties of selectively laser melted AlSi10Mg alloy

Larrosa, N. O.; Wang, W.; Read, N.; Loretto, M. H.; Evans, C.; Carr, J.; Tradowsky, U.; Attallah, M. M.; Withers, P. J.

DOI:

[10.1016/j.tafmec.2018.09.011](https://doi.org/10.1016/j.tafmec.2018.09.011)

License:

Creative Commons: Attribution-NonCommercial-NoDerivs (CC BY-NC-ND)

*Document Version*

Peer reviewed version

*Citation for published version (Harvard):*

Larrosa, NO, Wang, W, Read, N, Loretto, MH, Evans, C, Carr, J, Tradowsky, U, Attallah, MM & Withers, PJ 2018, 'Linking microstructure and processing defects to mechanical properties of selectively laser melted AlSi10Mg alloy', *Theoretical and Applied Fracture Mechanics*, vol. 98, pp. 123-133.  
<https://doi.org/10.1016/j.tafmec.2018.09.011>

[Link to publication on Research at Birmingham portal](#)

## **Publisher Rights Statement:**

Checked for eligibility: 13/11/2018

## **General rights**

Unless a licence is specified above, all rights (including copyright and moral rights) in this document are retained by the authors and/or the copyright holders. The express permission of the copyright holder must be obtained for any use of this material other than for purposes permitted by law.

- Users may freely distribute the URL that is used to identify this publication.
- Users may download and/or print one copy of the publication from the University of Birmingham research portal for the purpose of private study or non-commercial research.
- User may use extracts from the document in line with the concept of 'fair dealing' under the Copyright, Designs and Patents Act 1988 (?)
- Users may not further distribute the material nor use it for the purposes of commercial gain.

Where a licence is displayed above, please note the terms and conditions of the licence govern your use of this document.

When citing, please reference the published version.

## **Take down policy**

While the University of Birmingham exercises care and attention in making items available there are rare occasions when an item has been uploaded in error or has been deemed to be commercially or otherwise sensitive.

If you believe that this is the case for this document, please contact [UBIRA@lists.bham.ac.uk](mailto:UBIRA@lists.bham.ac.uk) providing details and we will remove access to the work immediately and investigate.

# LINKING MICROSTRUCTURE AND PROCESSING DEFECTS TO MECHANICAL PROPERTIES OF SELECTIVELY LASER MELTED ALSI10MG ALLOY

N.O. Larrosa<sup>1\*</sup>, W. Wang<sup>2</sup>, N. Read<sup>2</sup>, M. H. Loretto<sup>2</sup>, C Evans<sup>3</sup>, J. Carr<sup>3,4</sup>, U. Tradowsky<sup>5</sup>, M.M Attallah<sup>2</sup> and P.J. Withers<sup>3,4</sup>

<sup>1</sup> Department of Mechanical Engineering, University of Bristol, Bristol, BS8 1TR, UK

<sup>2</sup> School of Metallurgy and Materials, University of Birmingham, Edgbaston, Birmingham, B15 2TT, UK

<sup>3</sup> School of Materials, The University of Manchester, Manchester, M13 9PL, UK

<sup>4</sup> Henry Royce Institute, The University of Manchester, Manchester, M13 9PL, UK.

<sup>5</sup> Photon Laser Engineering, Staakener Str. 53-63, D-13581 Berlin, Germany

## Abstract

Here we analyse the relationship between the monotonic and cyclic behaviour of cylindrical AlSi10Mg (CL31 AL) samples fabricated by Selective Laser Melting (SLM) to the presence of manufacturing defects (pores, voids, oxides, etc.) and the beneficial effect of post-processing - T6 and hot isostatic pressing (HIP)- treatments. Correlative Computed Tomography (X-ray tomography, optical microscopy, electron backscatter diffraction, SEM and TEM) is used to characterise the microstructure and the three-dimensional (3D) structure of fatigue samples and to shed light on the role of defects on the experimental fatigue behaviour. Pancake-shaped pores are observed in the plane of the deposited layers having a 130% higher volume fraction for the vertical layering deposition (VL) than for horizontal layered (HL) orientations, and being larger and flatter. Further, while T6 treatment had relatively little effect on reducing porosity, the HIPping reduced the pore fraction by 44% and 65% for VL and HL samples, respectively. T6 and HIPping decreased the yield stress and the ultimate tensile strength considerably while increasing elongation and reduction of area accordingly. Although results are not conclusive and further work is required, our results suggest that the fatigue life seems to be dominated by the presence of these crack-like (pancake-like) defects perpendicular to the loading direction such that it is better to build samples transverse to the highest fatigue loads. Both T6 heat treatment and HIPping appear to reduce the fatigue strength of the material regardless of the AM deposition scheme as they tend to enlarge and collapse pores/voids to flat crack-like defects.

Keywords: Selective Laser Melting, Aluminium alloys, Porosity, Microstructure, Mechanical properties

## INTRODUCTION

Unlike conventional material removal (subtractive) manufacturing techniques, additive manufacturing (AM) technologies allow the production of near-net shape components by building up the material layer by layer as powder or wire is melted locally by a computer-controlled energy source.

Due to their potential to revolutionise the production of components, additive manufacturing techniques have experienced an exponential growth in the last two decades and there is great expectation on the benefits that these methodologies could provide a whole range of applications and industries. Components made by AM are already used in high performance automotive and aerospace industries. In Formula 1, for example, teams have been using AM to meet the challenges set by newly imposed rules and increased competition (1). In the medical device industry, 3D printed dental (2), orthopaedic and maxillofacial titanium implants have been constructed and used successfully. However, to date, most additive manufacturing applications have been focused on non-critical applications due to the fact that the mechanical behaviour of engineering components fabricated via these procedures is still not well understood. Structures are known to show significant anisotropy (based on the build orientation) and scatter in their as-fabricated mechanical properties (A). Thermal post-processing (including the use of hot isostatic processing) appears to enhance the ductility of the builds, but reduces the strength of the alloys (B).

Cracks usually initiate at microstructural discontinuities or manufacturing defects that locally elevate stresses and strains. Both microstructural discontinuities (3) and manufacturing defects both under monotonic (4)(5)(6) and cyclic loading (7)(8)(9) have been widely reported for AM components, increasing the risk of reduced tolerance to damage. Further the location and nature of these defects depend on the AM deposition scheme (10). One of the main challenges therefore for these novel manufacturing technologies and material systems is to meet the minimum mechanical performance envelopes of conventionally made components.

In many applications, fatigue is one of the main mechanisms of component failure. For example, over half of the mechanical failures of current aircraft components are attributed to fatigue (11). It is expected that AM components will present a minimum set of extreme values of defect number and sizes in order for these materials to have the minimum required damage tolerant behaviour (12).

Process-induced AM defects and microstructure variations can affect the tensile and toughness properties. Along with surface roughness and residual stresses, these defects have a detrimental effect on the cyclic behavior of the material. The fatigue life of Selective Laser Melting (SLM) additively manufactured parts is dominated by the presence of porosity (13). Fatigue cracks have been observed by time lapse X-ray CT to nucleate from internal and external defects (pores, lack of fusion, second phase particles, etc.) in parts made by selective electron beam melting (SEBM)(14). In this study surface breaking defects were found to be more detrimental than internal defects. Based on AM experiments on various metal alloys (15)(16)(17), processing parameters, such as scan speed, layer thickness, laser power, substrate material, and the properties of the powders (physical properties and granulo-morphometry) are known to affect the formation of porosity, and thereby to have a direct impact on the mechanical behavior of the material.

Current state of the art AM techniques are not capable of manufacturing components of sufficient quality for included porosity to be insignificant from a structural integrity viewpoint. The application of damage tolerance (DT) principles can offer a way to effectively introduce these materials into service by accounting for the presence of manufacturing flaws in the structural behavior both at the design stage and for monitoring

flaws during operation. The study of the effect of manufacturing parameters and post-processing thermo-mechanical treatments on porosity and their implications in the fatigue behaviour is thus paramount.

The aim of this paper is to correlate the fatigue performance of AM materials with the presence of manufacturing defects. With this aim in mind the results from fatigue tests of SLM AM specimens made from Al-10Si-Mg (CL31) powders are presented. The effect of two different layering orientations and three processing conditions, i.e. as-fabricated, after T6 heat treatment and after Hot Isostatic Pressing (HIP), on the fatigue life with respect to the 3D defect structure is assessed in this investigation. X-ray computed tomography (CT) is used to quantify the porosity in 3D on the micron scale in each case to evaluate the impact of layering strategies and post-processing treatments on controlling porosity. Experimental fatigue performance is then correlated to the different pore structures observed during CT using damage tolerance principles to shed light how the fatigue performance of AM parts might be improved.

## **METHODS AND MATERIALS**

### **Selective laser melting process (SLM)**

SLM is an AM process that builds parts by melting consecutive powder layers using a fibre laser. Specimens were manufactured on a Concept Laser M2 Cusing system (laser powder-bed fusion) at the University of Birmingham. The M2 system has an Ytterbium-fibre laser (1070 nm wavelength) with a power up to 400 W and a 60  $\mu\text{m}$  spot size. All processing was carried out in an Argon atmosphere with Oxygen content below 0.1%. A chequer-board (island) scanning strategy was used to fabricate the samples (see Figure 1), in which the layers are divided into several 5.6 mm square domains. Each domain is created basically by raster scanning of the laser beam. After selective melting of the domains, laser scans are carried out around the perimeter of the layer to improve the surface finish. For each subsequent layer, these domains are translated by 1 mm in the X and Y-directions and the scanning direction inside the islands is rotated by 90°. Samples were processed in two orientations. Vertically built (V) samples have layers (plane XY) with normal vector parallel to the cylinder axis (Axis Z); horizontally built (H) layers (Plane ZY) have their normal vector perpendicular to the cylinder axis (Axis X), as shown in Figure 1. All samples have a cylindrical geometry (55 mm long and 8 mm in diameter).

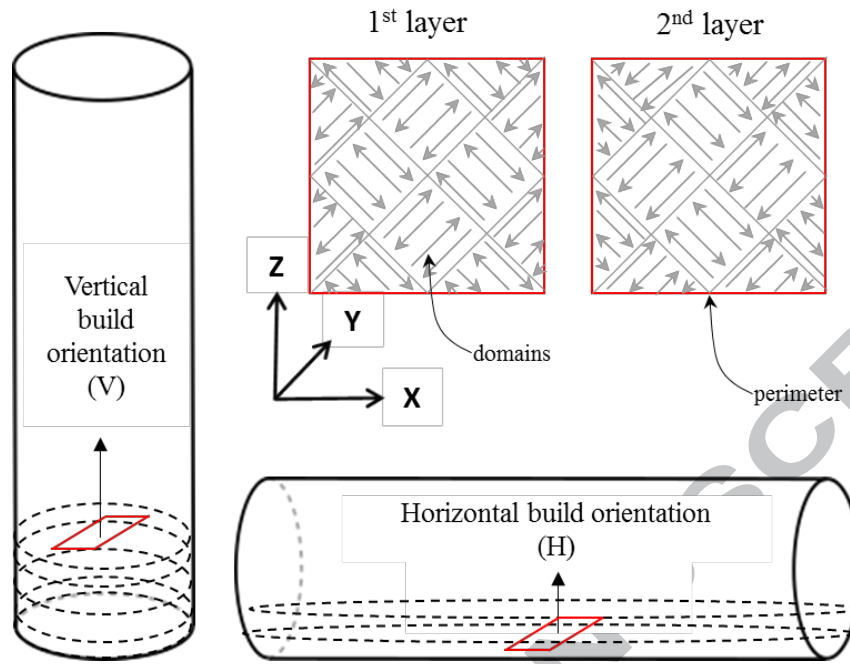


**Fig. 1:** The chequer-board technique for layer deposition. Cylindrical samples (55x8 mm) showing the build direction parallel (vertical build) or perpendicular (horizontal build) to the cylinder axis .

For AlSi10Mg, the effect of building parameters has been recently discussed by Aboulkhair *et al.* (13), Read *et al.* (18), and Tradowsky *et al.* (5). These authors studied the effect of scanning orientation, scanning speed and hatch spacing on the porosity of the part. Based on the optimum parameters indicated in this study, the following parameters are used to synthesize the samples: 175 W power; 1025 mm/s scan speed; 30  $\mu\text{m}$  powder layer thickness; and 97.5  $\mu\text{m}$  scan spacing. It is important to mention that, in contrast to the work reported herein, Aboulkhair *et al.* and Read *et al.* optimised the process parameters for non-spherical powders. However, as the aim of the current study is to assess the impact of post-processing rather than the parameters, the selected parameters were acceptable.

## Material

The powder used in this study was gas atomised AlSi10Mg with a size range of 25-50  $\mu\text{m}$ , supplied by TLS Technik. The composition is shown in Table 1. The particles are spherical with no internal porosity (5). The flowability, as measured using the Schulze ring test (19), was found to give a Flow Factor Classification (FFC) of 10.35, and the ratio of the tap to apparent densities (Hausner ratio),  $H = \frac{\rho_{\text{tap}}}{\rho_{\text{bulk}}}$  was 1.29, which are both indicative of good powder spreading behaviour, as required for SLM (20)(21).

Table 1: Chemical composition of AlSi10Mg powder

Element	Al	Si	Mg	Fe	Mn	Cu	Zn	Ti	Ni	Total
---------	----	----	----	----	----	----	----	----	----	-------

Nominal composition (wt. %)	Bal.	10.2	0.3	0.15	0.05	0.005	<0.002	0.015	0.012	100
-----------------------------	------	------	-----	------	------	-------	--------	-------	-------	-----

### Post-Processing

Post AM thermal processing is usually used to reduce porosity, thus reducing potential crack initiation sites, and therefore increasing fatigue life. Some authors (21),(22) have reported hot isostatic pressing (HIPing) to be very effective at closing porosity in Ti6V4Al. In previous work (22) it was found that HIPping is also effective in closing porosity in AlSi10Mg, although subsequent heat treatments were found to reopen some of the apparently closed pores in aluminium and titanium (24). As a result, the effect of HIPping on fatigue behavior is also studied here. HIPping was applied using an EPSI HIP vessel using the conditions summarized in Table 22. In addition, the effect of solution + peak aging heat treatments (T6) as described in Table 22, the standard heat treatment for cast AlSi10Mg, is also considered. An electrically heated furnace from LTD was used for T6. A combination of HIPping followed by T6 heat treatment was performed on some of the samples. One sample for each condition shown in Table 3 was examined.

Table 2: HIP and T6 aging treatment parameters

HIP Parameters			
Temperature	Pressure	Time	Heating- / Cooling Rate
530°C	100 MPa	2 h	5°C/min
T6 Parameters			
Solution HT		Aging HT	
520°C/5 h/Water quenching		160°C/12 h/air cooling	

Table 3: The AM layering orientations and heat treatments of the six samples.

Layering	Heat treatment		
Vertical (V)	As Fabricated (AF)	T6	HIP
Horizontal (H)	As Fabricated (AF)	T6	HIP



### 3. Imaging characterisation of microstructure and porosity

#### 3.1 Microstructural Characterisation

Samples were examined optically (OM), using scanning electron microscope (SEM) and a transmission electron microscope (TEM).

##### 3.1.1 Optical Microscopy (OM)

For optical microscopy, samples were cut along the XY plane, showing the laser scan directions, and the YZ plane (parallel to the building direction). After polishing to a 0.04  $\mu\text{m}$  oxide polishing finish, NaOH solution (2g NaOH in 100 ml  $\text{H}_2\text{O}$ ) was used to etch the samples. The as-polished samples were examined using a Zeiss Axioskop2 optical microscope (OM) to determine the void content through image analysis using ImageJ Software (25). The etched samples were examined using Leica LEITZ DMRX OM. The micrographs from the polished XY sections of the AF 0° sample in Fig. 2 show big irregular voids and small spherical voids. There are two types of voids, spherical voids caused by the entrapped gas and irregular voids, which are likely to be oxide film defects. It is observed that spherical voids are much smaller ( $<20\text{ }\mu\text{m}$ ) than the irregular voids.

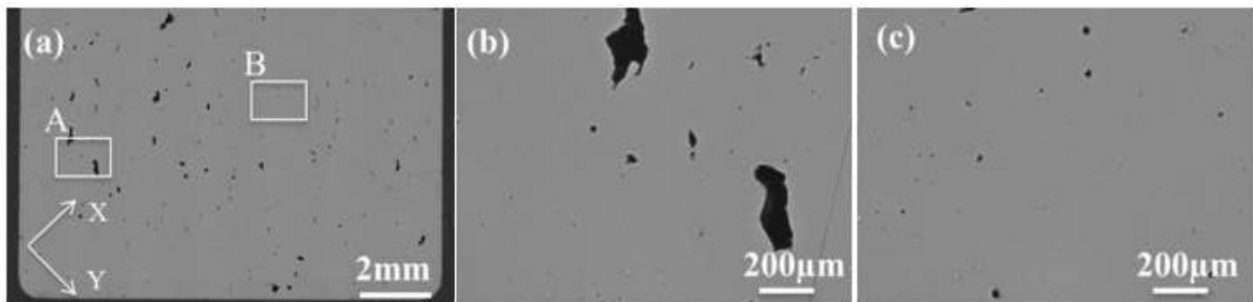


**Fig. 2.** Optical micrographs of XY plane of AF 0° sample at (a) low magnification and higher magnification (b) area of A and (c) area of B as shown in (a).

Figure 3 shows a cross-section of a horizontally grown sample where the void content changes with the build height. More irregular voids can be observed in the bottom half than the top half. As a result, the void content in the bottom half is  $\sim 1.7$  area% which is almost twice that of the top half (of about 1 area %). Meanwhile, it is worth to mentioning that the void content of irregular voids does not vary too much with the building height in the vertical sample since the geometry of each layer does not change with the building direction, while the horizontal sample does.

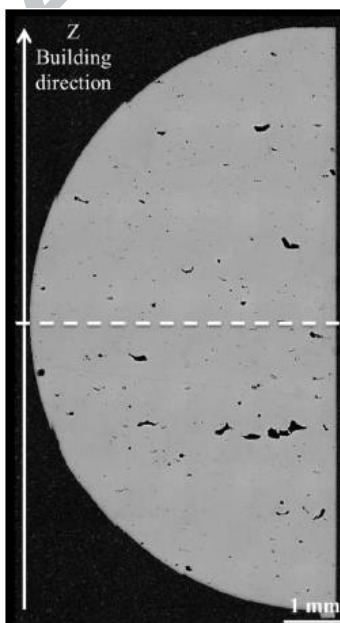


**Fig. 3.** Optical micrograph showing an YZ cross section of half of a AF 0° bar. The white dashed line marks the diameter of the cylindrical sample.

Figure 4 shows optical micrographs for the etched cross-sections of the YZ plane in the AF, T6, and HIPped samples, built in different directions. Fig 4a-b show half cylindrical shape molten pools and few voids. However, after T6 heat treatment these patterns are not obvious (Fig 4 d-e) and some gas pores have enlarged due to the

thermal expansion. Fig 4f and 4g show HIPped samples where the half cylindrical shapes are also no longer obvious and the void content has been reduced.

### 3.1.2 Scanning Electron Microscopy (SEM)

A JEOL 7000 SEM fitted with INCA EBSD was used. The grain size, the size and volume fraction of Si second phases were measured on etched T6 and HIPped samples. The fracture surfaces of the tensile and fatigue samples were also examined.

Figs. 5a-c show typical SEM micrographs of the AF microstructure. In the low magnification image shown in Fig. 5a, the edge of a laser molten pool can be seen. Fig. 5b shows a fine cellular microstructure adjacent to a region with a similar, but finer microstructure. A higher magnification image taken from the coarser region in Fig. 5b is shown in Fig. 5c where a coarse phase is visible between the cell-like regions, which are about 350nm in diameter. Some of these regions appear to contain fine particles, but they are too fine to be characterised in SEM. Some small gas voids (0.5-1.0µm) are visible as the black dots in these images.

Figures 5d and 5e show the microstructures after T6 heat treatment where a high density of precipitates can be observed. Precipitates are large enough to be identified as Si precipitates using energy-dispersive X-ray analysis (EDX). The fine microstructure obvious in the AF sample is no longer present. Some larger spherical voids are also now visible. The microstructure after HIPping (Fig. 5f), is similar to that after T6, but the spherical gas voids are no longer visible. However, HIPping does not fully close the irregular voids, as shown in Fig. 5g.

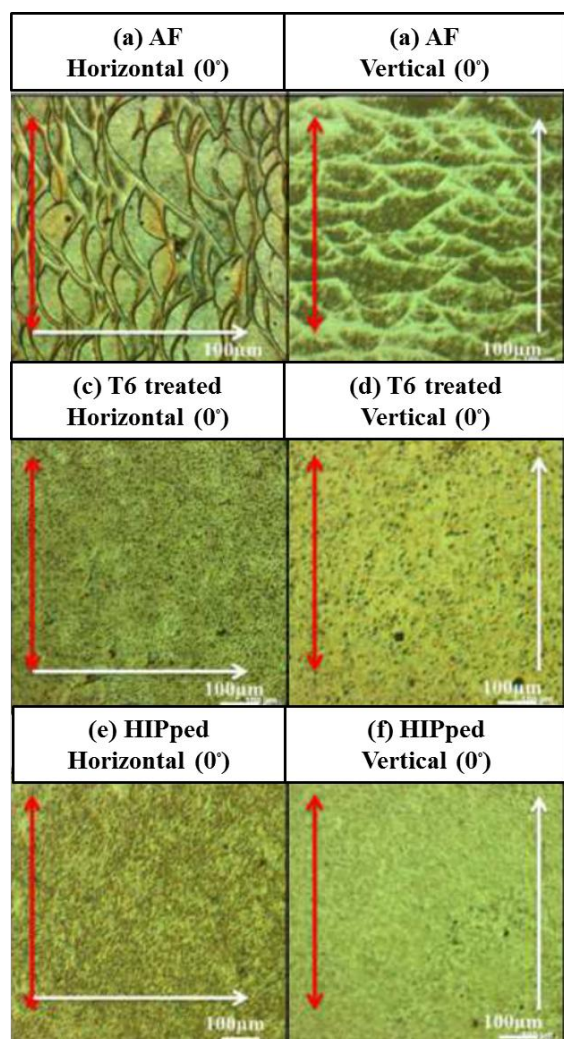


**Fig. 4.** Optical micrographs of (a) AF Horizontal (0°), (b) AF Vertical (90°), (c) T6 treated Horizontal (0°), (d) T6 treated Vertical (90°), (e) HIPped Horizontal (0°) and (f) HIPped Vertical (90°) sample. White arrows indicate the building direction. Red arrows indicate the loading direction in tensile samples.

The development in Si precipitates size in the T6 and HIPped samples is shown in Fig. 6. The distribution of Si precipitates in the AF sample (see Fig. 5c) did not result in meaningful results (as discussed later). The data shown in Fig. 6 was obtained from about 1000 particles in the T6 sample and from about 2000 particles in the HIPped sample from the analysis of SEM images of each sample. There is a significantly higher fraction of particles in the 0.5-1.5 µm range in the HIPped sample compared to that in the T6 sample and the maximum size of particles is under 4 µm and 5 µm in the HIPped samples and T6 samples, respectively. This difference in the extent of particle coarsening, which occurs during holding for 2h at 520°C (during HIP) and for 5h at 530°C (during T6 treatment), is expected since particle coarsening is



proportional to time and will increase at the higher temperature (28). In addition, the HIP pressure will also decrease diffusivity and thus the rate of particle coarsening. Some fine needle like precipitates, which contain Mg and Fe are seen in the T6 samples (see Fig. 5e). The coarsening of the Si precipitates is likely to result in a significant drop in strength in the HIPped samples, although these precipitates in the T6 samples will increase the yield stress as discussed later.

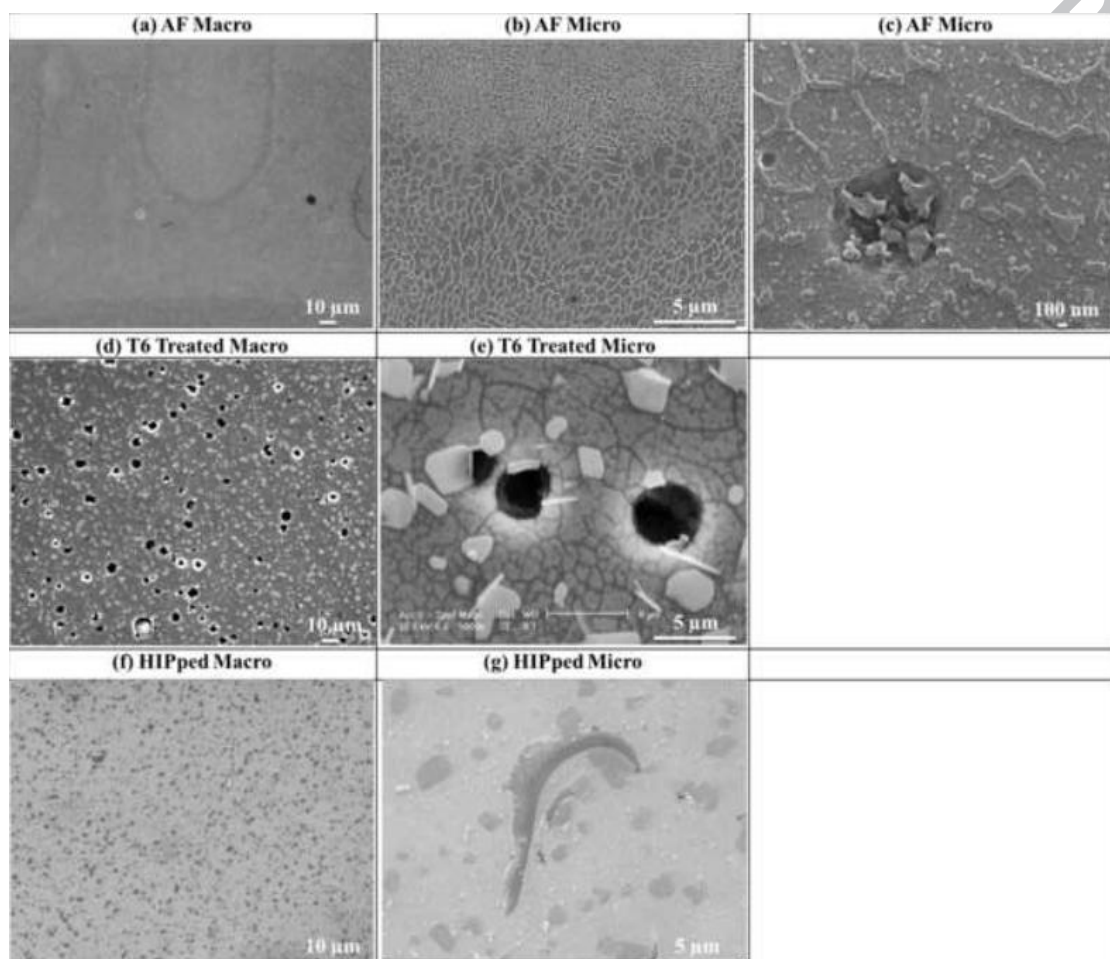


**Fig. 5.** Secondary electron SEM images of XY sections. (a), (b) and (c) AF, (d) and (e) T6 treated and (f) and (g) HIP treated samples of AlSi10Mg.

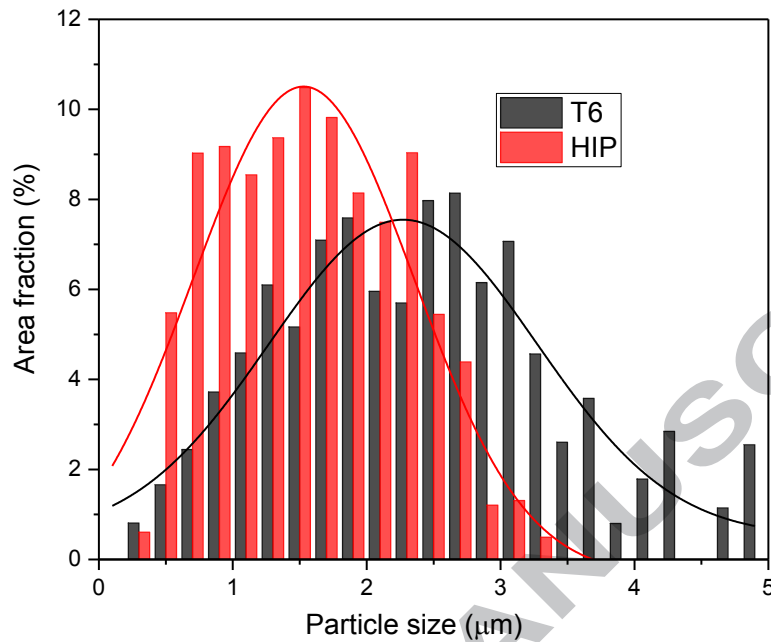


Fig. 6. Silicon (Si) particle size distributions of T6 treated and HIPped samples. Particles below 300nm not included due to limitations in resolution.

The crystallographic orientation of the grains in the YZ and XY sections, formed during SLM is shown for AF samples in Fig. 7a and b. The YZ section (Fig. 7a) shows that the grains grow perpendicular to the melt pool border towards the centre of the melt pool. The shape of the melt pool is elongated as a result of the moving laser. Hence, as Thijs et al. (27) pointed out, the laser scanning strategy has a strong influence on the directionality of the solidification and further affects the texture. The island laser scan strategy gives rise to a chess pattern in the XY plane in the EBSD map of the AF sample (Fig. 7b). Grain size distributions in samples obtained from images such as those in Fig. 7(b) are shown in Fig. 8. The average grain size in the AF sample is 2.7μm. In the T6 sample, the average grain size is 3.1μm. The average grain size in the HIPped samples was about 3.4μm.

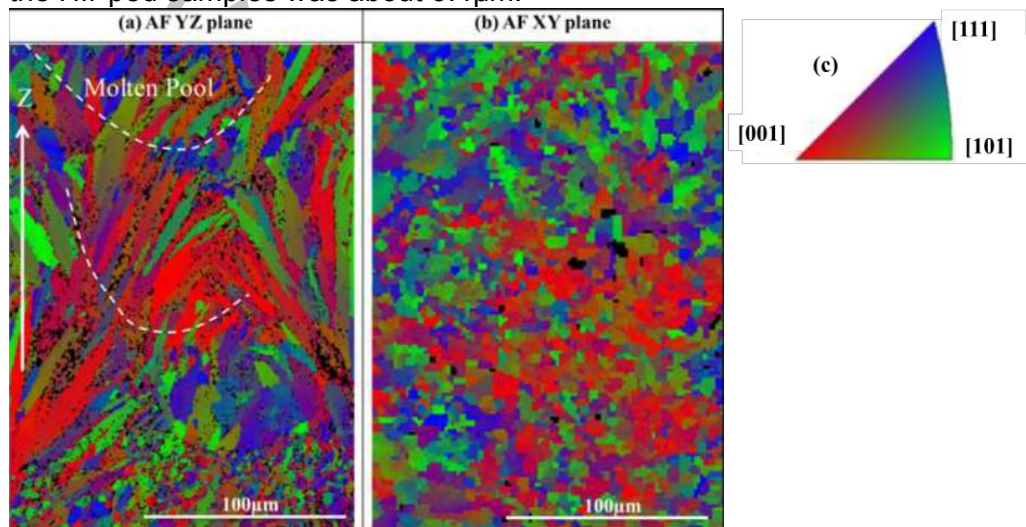


Fig. 7. Coloured EBSD orientation image maps of (a) YZ plane (parallel to the building direction) & (b) XY plane (perpendicular to the building direction) of AF vertical sample. (c) Inverse pole

Fig. (IPF).

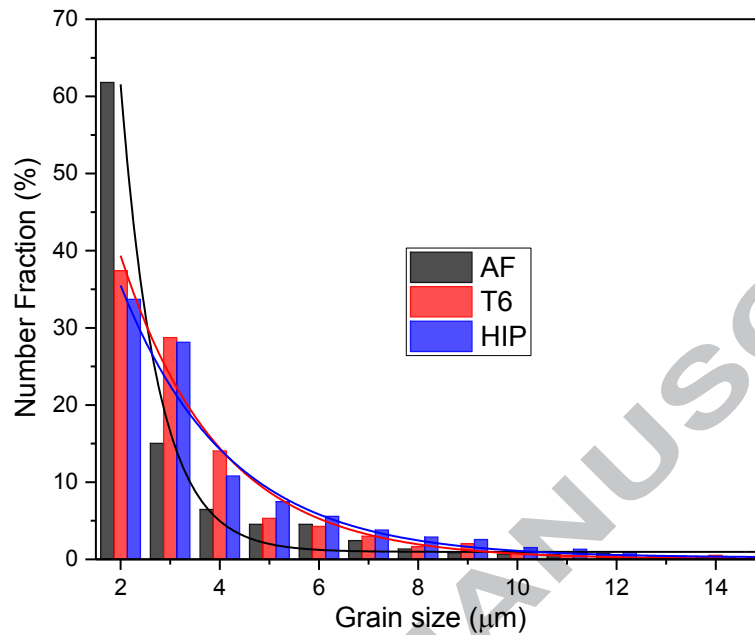


Fig. 8. Grain sizes on XY plane of AF, T6 treated and HIP treated sample. Solid lines show exponential fitting.

### 3.1.3 Transmission Electron Microscopy (TEM)

TEM samples were extracted from the XY plane in the AF samples using spark machining and prepared by electro-polishing in a 10% vol.  $\text{HClO}_4$  in  $\text{CH}_3\text{OH}$  solution, followed by cleaning using PIPS (Precision Ion Polishing System). Investigations of the solidification substructure were performed using a JEOL 2100 TEM operating at 200kV, equipped with Energy Dispersive X-ray Spectroscopy (EDX) system.

Figure 9a shows a low magnification bright field TEM micrograph after tilting to a condition where many adjacent fine cells, spanning distances up to about  $5\mu\text{m}$ , show similar dark contrast, whereas other regions are far brighter. The individual cell-like regions are about 350 nm in diameter. Higher magnification images are shown in Fig. 9b and d together with diffraction patterns, in Fig. 9c and 9e taken from the areas indicated by the pointer. Identical micro-diffraction patterns were obtained from within the dark area in Fig. 9b, as shown in the two patterns in Fig. 9f, which were taken from within this dark region.

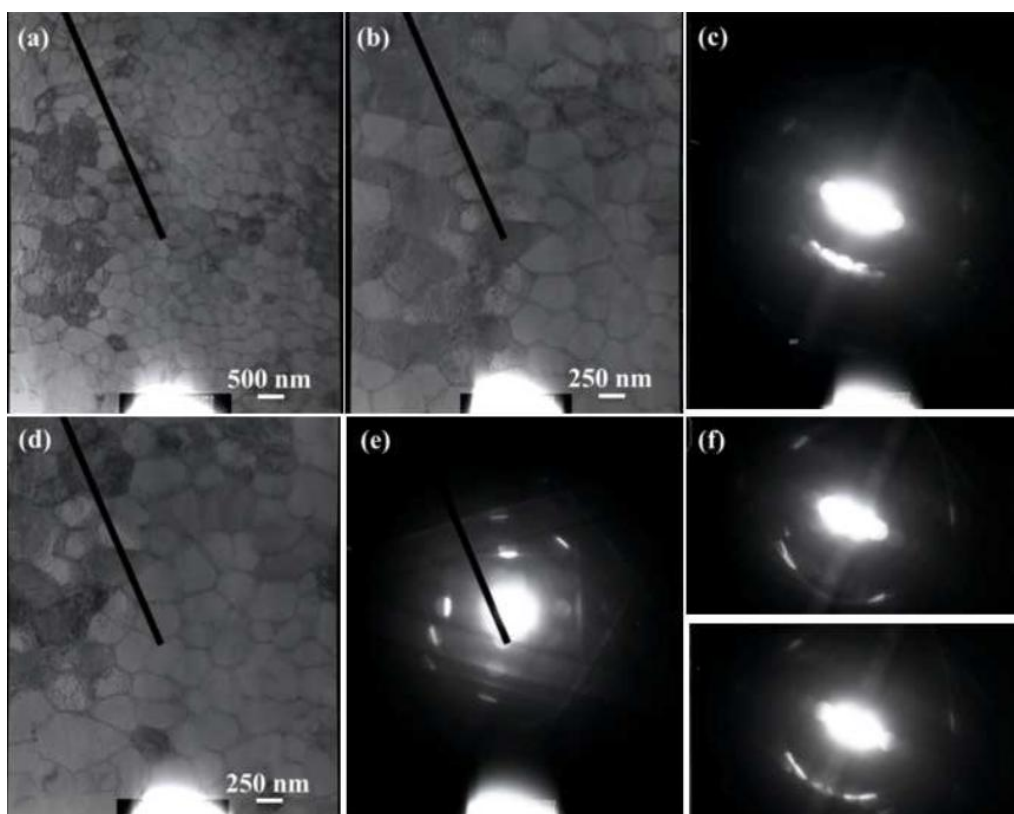


Fig. 9. Bright field TEM images of an XY section of electropolished and HIPped AF sample. (a) Low magnification, showing cells of different intensity. In (b) the cell indicated is close to, the Bragg angle for  $\mathbf{g}$  (diffracting vector)  $=111$  as shown in the diffraction pattern in (c) taken from the region indicated by the pointer. The diffraction conditions for the region indicated by the pointer in (d) are shown in (e) where no low order  $\mathbf{g}$  is close to Bragg. The (identical) inset diffraction patterns in (f) were typical of those taken from different cells within the dark region shown in (b) after tilting slightly about  $\mathbf{g}$ . There is no rotation between the images and diffraction patterns.

The dark contrast arises when a region is imaged close to the Bragg angle and tilting away from the Bragg condition, to kinematical conditions, results in an increase in intensity in a bright field image (29). The bright regions dominate because kinematical conditions do not require a specific orientation to be selected, whereas a strong reflection must be excited if a region is to be strongly diffracting.

These observations show that the cells are grouped in clusters which are typically about  $3\mu\text{m}$  diameter and which all show similar contrast, when imaged close to the Bragg condition, are all part of one Al grain. This is consistent with the EBSD map of the XY section shown in Fig. 8b, where the grain sizes range from 1 to about  $5\mu\text{m}$  although most are below about  $5\mu\text{m}$ .

EDX analysis has been carried out in STEM and TEM on the AF sample, which showed, as expected from the analyses in SEM, the boundaries of the cells are very high in Si and in thinner regions the Si content is measured at virtually 100% Si, although Mg and Fe at about the 0.5 at. % level were occasionally detected in these Si particles. The composition of the Al matrix in the cells was measured and was about 2 or 3at. % Si but this was accompanied by about 2 to

3at. % O, which suggests that the Si signal may be associated with a film of SiO<sub>2</sub> from electropolishing.

TEM observations of the T6 and Hipped samples showed as expected a significant density of fine Si precipitates, down to below 10nm in the T6 samples, but only large precipitates in the HIPped samples. As noted earlier measurements of the sizes of such small precipitates in this alloy is difficult in SEM.

### 3.2 Characterisation of the porosity by X-ray Computed Tomography (X-CT)

Finally, AM samples were scanned at the Henry Moseley X-ray Imaging Facility using a ZEISS Xradia Versa 520 CT system. For each sample, 1601 projections were collected with exposure times of 3 s. The X-ray source energy was set to 80 keV and a power of 7 W combined with the LE4 filter to enhance the transmission through the sample. The relative source, sample and detector distances, coupled with the 0.39x detector with no pixel binning gave a native pixel size of 6.1  $\mu\text{m}$ . Projections acquired using these settings produced >4500 counts and >40% transmission within the centre of the sample.

Porosity is quantified using Avizo 9<sup>®</sup> software to perform connected component labelling on the segmented porosity (29). This is performed on a sub-volume measuring 300 by 300 by 300 pixels with a 12.1  $\mu\text{m}$  pixel size. Single pixel 'pores' are removed from the analysis. The sub-volume considered is from an identical location from each sample. The sub-volume was taken from the bulk of the AM specimens to represent porosity within the material after machining of the fatigue test samples. Volume distributions can be obtained from counting the connected voxels and multiplying by the voxel volume. Pore volume fractions are simply the total volume divided by the volume of the region of the analysed image. Effective diameters of the pores are calculated by assuming the volume,  $V$ , of the connected voxels form a sphere. We use the standard definition of sphericity,  $\Psi$ , to quantify shape by measuring the surface area,  $A$ , of a connected region and applying the following equation:

$$\Psi = \frac{\pi^{1/3} (6V)^{2/3}}{A} \quad (1)$$

3D renderings of the X-ray CT datasets were also obtained in Avizo 9<sup>®</sup> by surface meshing the output of the connected component labelling. Figure 11 shows a render of porosity for the 6 different samples. The influence of deposit layering orientation on porosity as well as the orientation of pores with respect to the cylinder longitudinal direction can be readily observed and compared from one layering strategy to the other. There is no clear evidence from the figure that T6 has any significant effect on reducing porosity although it seems that the application of HIP+ T6 may result in more dense parts. From fractography analysis in (5), oxide-induced voids were observed on the as-fabricated fracture surfaces. In addition, Figure 10 shows flat (oblate) pancake-like pores distributed perpendicular to the layering directions. Thus, in general pancake pores/voids are oriented parallel (H) or perpendicular (V) to the cylinder axis, or in other words to the fatigue loading direction, depending on the layering deposition strategy.



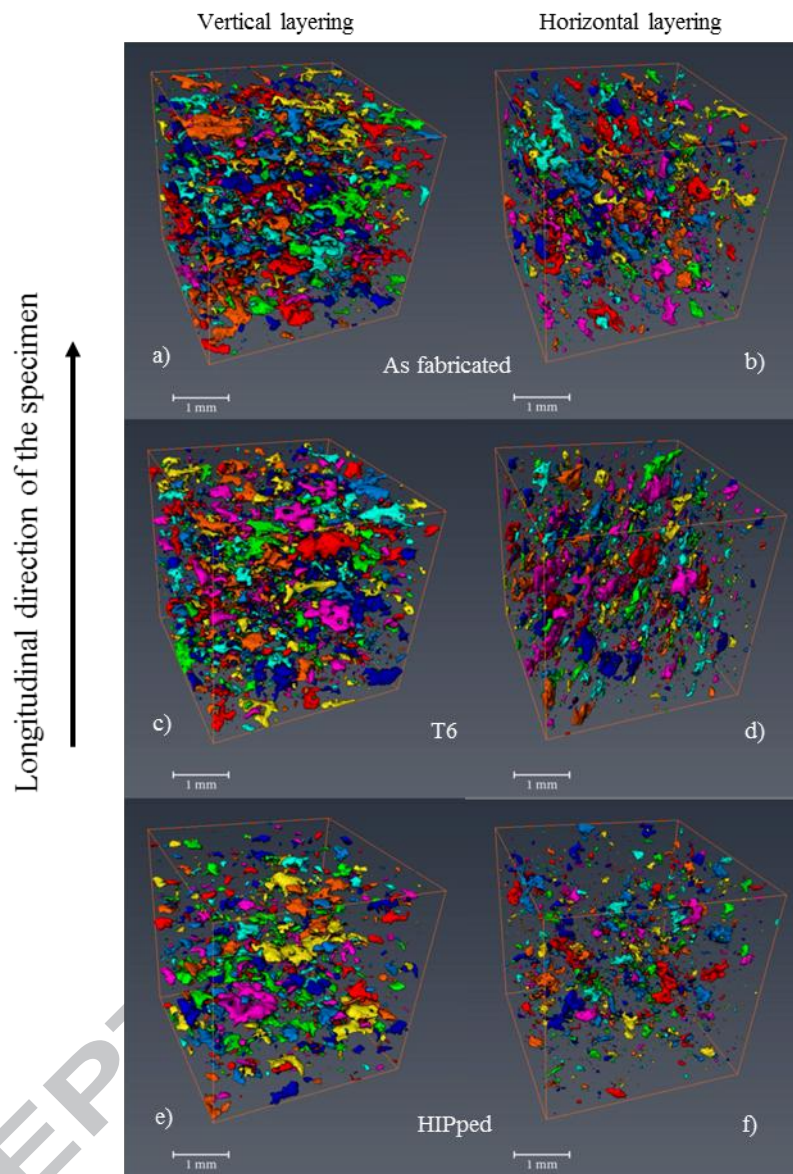


**Fig. 10:** 3D rendering of the segmented pores in a region of interest for the different conditions. The false-colour coding is used only to improve clarity.

Table 4 shows the total pore fraction of each sample, as determined from the segmented sub-volumes in Fig 10. A marked difference in the volume fraction between the HL and VL samples is observed both qualitatively from Fig 10 and quantitatively from Table 4, with the VL sample containing more than double the volume fraction of pores (despite a similar number of pores) compared to the HL sample. No significant difference is observed after the T6 treatment. It is evident that HIPping reduced the number and volume fraction of pores (by 50%) for the VL deposited sample, and if anything is even more effective at reducing the pore fraction in the HL case (approximately a two thirds reduction). This may be because the microstructure is more amenable to HIPping in this orientation, leading to just 0.7% porosity after HIPping in this case. This trend agrees with SEM observations in Fig 5.

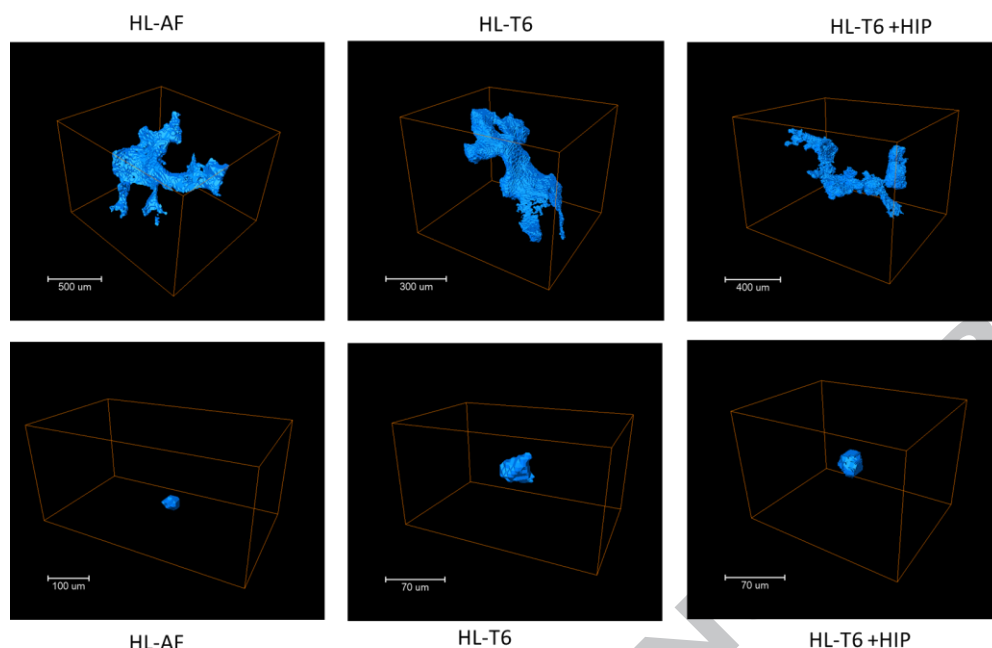
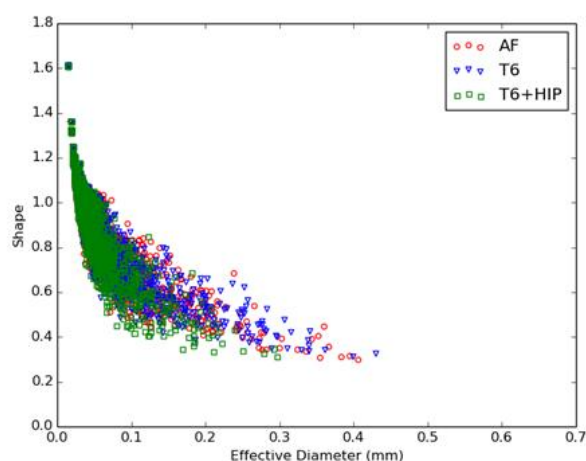
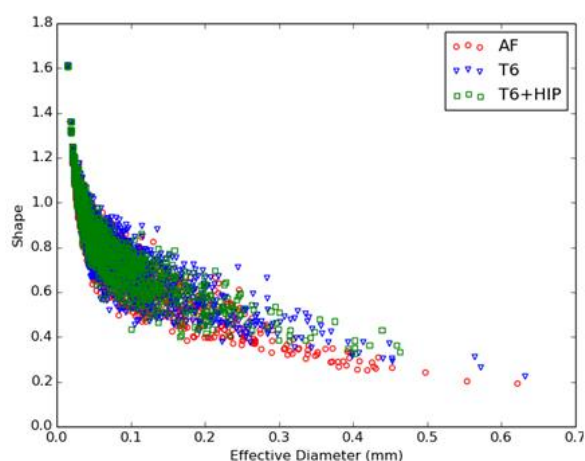


**Fig. 11:** 3D rendering of segmented pores at different conditions. Horizontal layering.

Figure 11 shows examples of spherical and flat pores in a HL sample. The difference in size and shape is evident (note the difference in scale). There appears to be a relationship between size and shape as the spherical pores are several orders of magnitude smaller than the penny pores.

Table 4: Total pore fraction (%) and pore density. Percentage differences with respect to AF are shown in brackets.

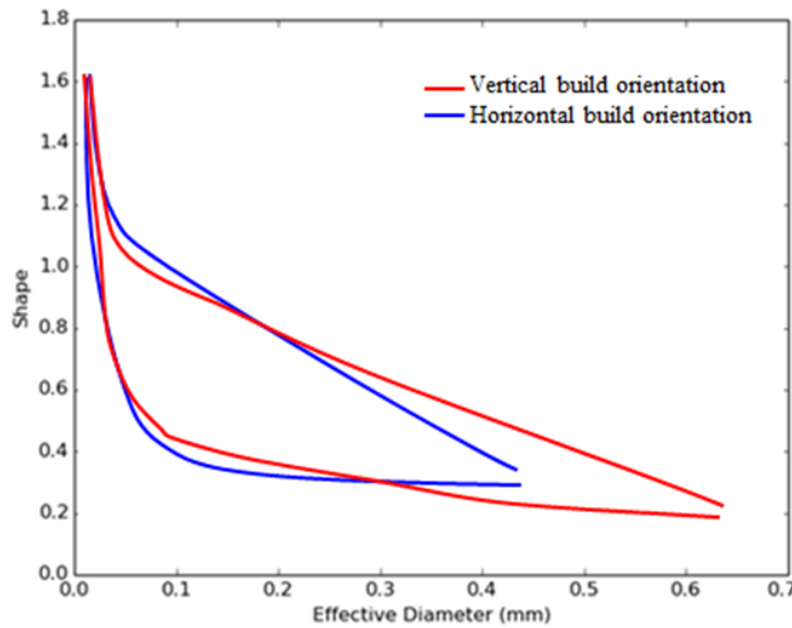
	Total pore fraction (%)		Number of pores per mm <sup>3</sup>	
	VL	HL	VL	HL
<b>AF</b>	4.6	2.0	69.0	70.9
<b>T6</b>	4.6 (0%)	2.2 (13%)	78.2 (13%)	77.3 (9%)
<b>HIPped</b>	2.6 (-43%)	0.7 (-65%)	30.7 (-56%)	58.4 (-18%)



**Fig 12:** A scatter plot of the shape factor (sphericity) against the effective diameters for the VL(left) and HL (right) samples.

Figure 12 is a scatter plot of the effective diameter and corresponding shapes of each pore in the ROI. For Vertical (V) samples, it is observed that the sphericity (shape) of pores in the AF samples (red open circles) tend to be lower than those in the other two conditions and this is particularly evident for larger pores (high effective diameters). For this layering orientation, the shape factor is higher for both T6 and HIPped conditions, i.e. pores are 'less flat'. It is also observed that there is not significant difference in pore dimensions from samples in AF and T6 conditions (maximum value close to 0.6 mm). In contrast, samples with HIP+T6 show reduced diameter (maximum value close to 0.45 mm).

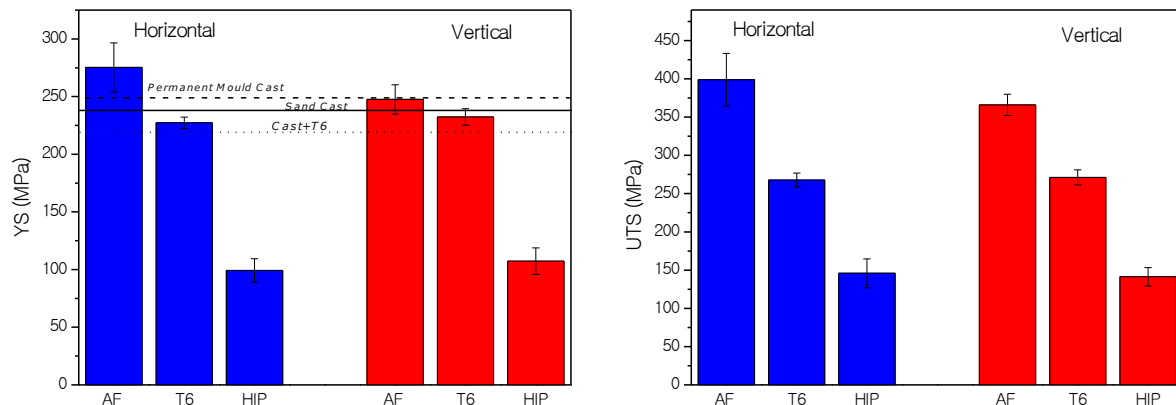
Figure 13 shows the envelope curves for the point clouds in Fig. 12 for the two different build orientations, irrespective of heat treatment. The figure shows that VL samples have larger and flat pores ('pancake-like') compared to HL samples, which seem to have fewer and smaller pores.

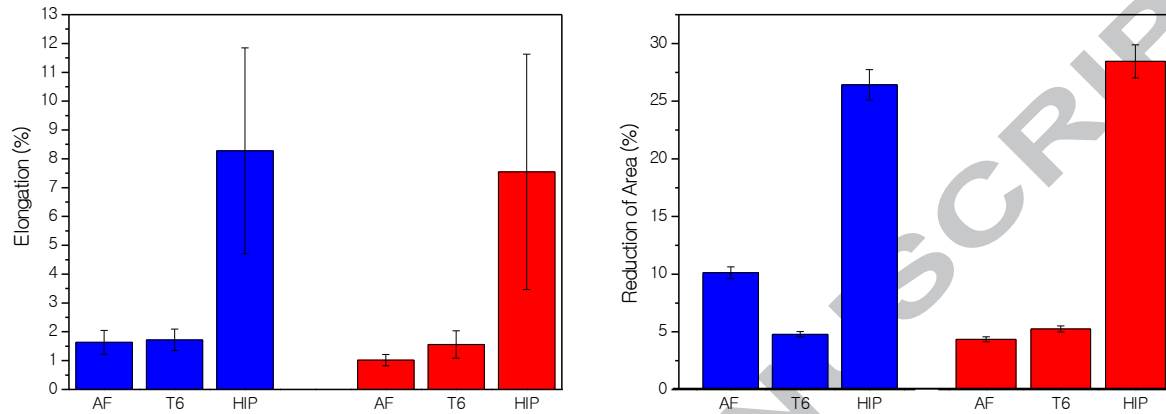


**Fig.13:** Shape factor (sphericity) against the effective diameters for different layering orientations.

## 4 Mechanical experiments

### 4.1 Tensile tests





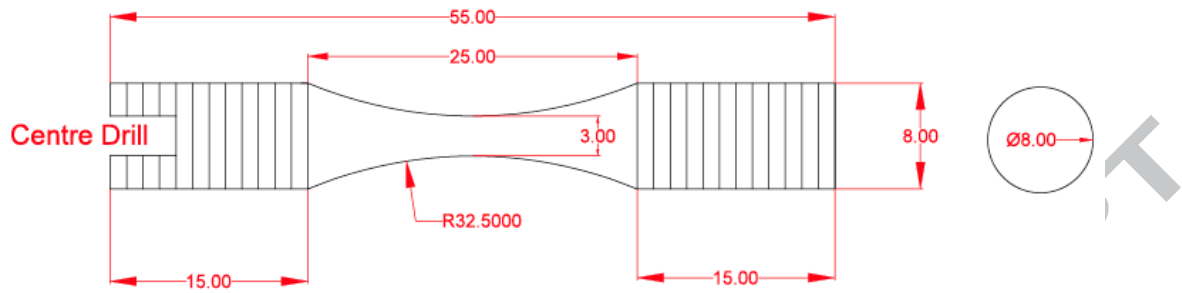
**Fig. 14.** The mechanical properties of the AF, T6, and HIPped samples, (a) YS, (b) UTS, (c) % Elongation (d) R.o.A for the various samples

Figure 14 shows the yield strength (YS), the ultimate tensile strength (UTS), elongation and reduction of area (R. of A.) to fracture in tensile tests for the HL and VL orientation samples in the AF, the T6, and HIPped conditions. Significant scatter is observed in most of the measurements. As expected, Yield Strength decreases for all samples from the AF value both after T6 heat treatment and after HIPping with the bigger change in the HIPped samples. In addition the elongation at fracture increases after HIPping. Actual stress strain curves from these samples show a high work hardening rate in the AF samples (5).

The failure of most samples appears to be initiated at the surface and as would be expected most cracks initiated from voids, some of which are surface-connected. The average ductility is less than 2% in the AF horizontal samples and after HIPping this increases to about 8% suggesting that failure is associated with volumetric defects, especially the large irregular voids in the AF samples.

#### 4.2 High Cycle Fatigue tests

High cycle fatigue (HCF) tests were performed for the AF and T6 treated horizontally and vertically built samples at different stresses ( $\Delta\sigma = 80, 115, 150, 185$  and  $220$  MPa), with one sample for each condition. The fatigue samples were machined according to ASTM E466 (30). They were fatigue tested according to EN 6072 at room temperature on a Wöhler type fatigue rotating bending machine (31). Samples were machined from ALM AlSi10Mg rods in the different conditions. A schematic of a fatigue sample geometry is presented in Fig. 15. All samples were ground to 4000 grit and polished to  $\frac{1}{4}$   $\mu\text{m}$  finish using diamond paste.



**Fig. 15:** Sample dimensions (in mm) for the fatigue test specimens.

The fatigue lives for one sample in each build orientation in AF and T6 conditions are plotted in Fig. 16 in logarithmic form. Life ( $\sigma_{\max}$ ), i.e.  $\sigma_{\max} = \sigma_{\min}/0.1$ , is reduced in the T6 samples from the values found in AF samples built both at VL and HL to the substrate. As expected, in general, the VL samples show a poor fatigue resistance compared to the HL samples, however this difference is not significant. This is thought to be due to the orientation of the pores with respect to the loading direction, where very flat pores perpendicular to the loading direction create high stress concentrations from which fatigue cracks can propagate. T6 shows to produce no benefit in terms of fatigue life at any stress level.

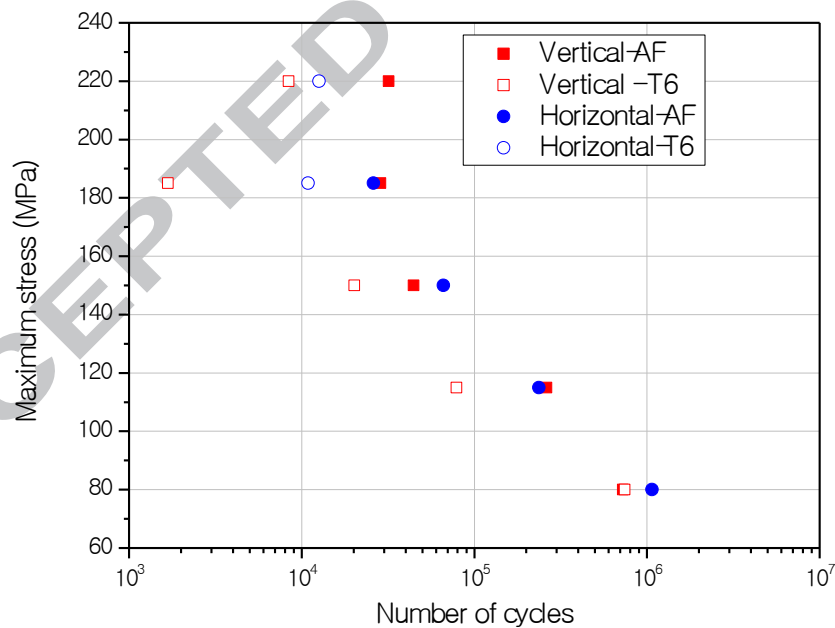


**Fig. 16.** S-N diagram of the AF and T6 treated samples.

In addition, a set of fatigue tests were performed for one sample in each build orientation and heat treatment condition. From the monotonic loading results in Section 4.1, differences in



ductility, yield strength and tensile strength were observed to be significant. Consequently for the fatigue tests to be comparable relative to the yield stress, the applied stress at which each sample was tested was derived using the concept of fatigue ratio. The fatigue ratio relates the fatigue strength to the tensile strength of the material. For many materials, the fatigue ratio is used in practice to estimate fatigue properties from data obtained in tension tests. In our case, we use it to estimate the level of cyclic stress to be used in the test. In our tests, the maximum stress in the fatigue cycle is 60 % of the average 0.2 % proof stress taken from tensile tests. Results were also compared to conventionally cast AlSi10Mg (5) (26). A cyclic frequency of 20 Hz and a stress ratio of  $R=0.1$  were used.

As also shown in Fig 16, VL samples show a poor fatigue resistance compared to the HL samples despite the much lower stress amplitudes to which they have been subjected. This is also related to the orientation of the pores with respect to the loading direction, where very flat pores perpendicular to the loading direction create high stress concentrations from which fatigue cracks can propagate.

The as-fabricated VL sample failed after over 7900 cycles which can be considered as low-cycle fatigue from the point of view of cycles. An increase in fatigue life by over 2,000 (28%) cycles upon heat treating to the T6 condition was observed. Hot isostatic pressing in conjunction with the T6 heat treatment increased the fatigue life by over 14,000 cycles (180%) over the as-fabricated sample. It is worth mentioning that due to having test only one sample in each condition we have no indication of scatter for the tests performed. This will be investigated in the future.

Building samples using a horizontal build direction produced a large increase in fatigue life for the as-fabricated sample. The horizontal AF sample exhibited an increase of 38,000 cycles over the vertical AF sample. For the horizontal build direction, the as-fabricated sample failed at over 46,000 cycles and T6 specimen failed at 171,000 (272% increase with respect to AF), 60,000 cycles later than the HIP+T6 specimen, which failed at 109,000 cycles (135% increase with respect to AF). This result is contrary to the expected benefit from performing an additional heat-treatment to the sample, and further testing is required in order to establish whether this is an anomalous result or some sort of defect collapse has been produced after HIPping. One explanation for this lower fatigue performance of HIPped HL sample could be that flat pores which were previously aligned with the load direction and not much influencing load-bearing capacity of the sample may have been rounded and increased the local stress level closed in the pores vicinity.

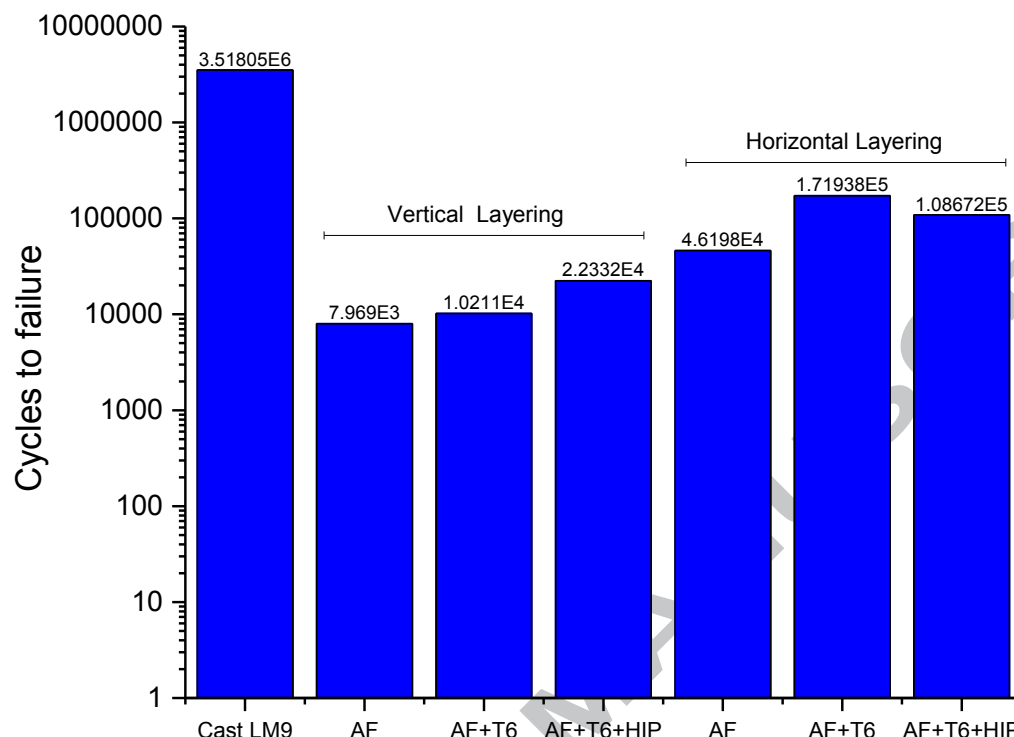


Figure 17: Fatigue lives for one each build direction (stress amplitudes 60% of 0.2% yield stress) and heat treatment combination (note log scale).

## CONCLUSIONS

Microporosity is formed during the SLM process as a result of lack of fusion in the layering deposition process, shrinkage and gas evolution during solidification. Pores act as stress/strain concentrations promoting crack initiation and propagation. Therefore, the effect of porosity in the structural integrity of fatigue-critical AM parts must be accounted for. In this study, the effect of heat treatment and AM build orientation on porosity and the associated mechanical behaviour were investigated for AlSi10Mg SLM AM cylindrical samples. The samples built parallel to the axis of the cylindrical samples (HL) showed significantly lower porosities than those built with the layers built up perpendicular (VL) to the axis.

In general, post-processing using T6 heat treatment followed by HIPping was able to reduce the porosity produced during the build by 44% for the vertical build and by 65% for the horizontal build, however mechanical properties have not been improved accordingly. The beneficial effect of T6 only is not so evident and further study is required. The YS of AF SLMed AlSi10Mg is high because the Al grains contain cell-like regions of about 350nm

diameter, that are surrounded by 10nm thick regions of Si, which inhibit dislocation motion within the larger (about 5µm cross section in XY plane) Al grains.

Pancake shaped pores are believed to act as fatigue crack initiators significantly reducing the life of the VL samples for which the plane of the pores is normal to the fatigue load, relative to those built horizontally for which the pancakes are edge-on to the fatigue load. Although experimental results were not conclusive though, some trend is observed, and for the material investigated porosity act as a fatigue reduction feature. This explains why AM samples with layers running parallel to the loading direction (HL), as opposed to perpendicular (VL), exhibit a better fatigue performance and may also explain the reduction in fatigue performance in the Hipped HL sample.

### Acknowledgements

This research was supported by the EPSRC (grants EP/K004530/1 and EP/J021229/1). We would also like to acknowledge the assistance provided by the Manchester X-ray Imaging Facility, which was funded in part by the EPSRC (grants EP/F007906/1, EP/F001452/1 and EP/I02249X/). PJW is grateful for an ERC grant (ADG 2015 EU project 695638 - CORREL-CT).

### REFERENCE LIST

- (1) Cooper D. E., Stanford M., Kibble K.A., and Gibbons G.J., *Mater. Des.*, Vol. 41, 2002, pp. 226–230.
- (2) Kruth, J.P. and Vandenbroucke, B. and Vaerenbergh, J. van and Naert, I. Rapid Manufacturing of Dental Prostheses by means of Selective Laser Sintering/Melting. *Proceedings of the AFPR*, S4, 2005.
- (3) Book, T.A., Sangid, M.D. *Mater Charact*, Vol 122, 2016, pp. 104-112.
- (4) Wu, J., Wang, X.Q., Wang, W., Attallah, M.M., Loretto, M.H. *Acta Mater*, 2016, Vol 117, pp. 311-320.
- (5) Tradowsky, U., White, J., Ward, R.M., Read, N., Reimers, W., Attallah, M.M. *Mater Design*, 2016 Vol 105, pp. 212-222.
- (6) Qiu, C., Panwisawas, C., Ward, M., Basoalto, H.C., Brooks, J.W., Attallah, M.M. *Acta Mater*, 2015, Vol 96, pp. 72-79.
- (7) Razavi SMJ, Ferro P, Berto F. *Materials* 2018, 11(2), 284.
- (8) Razavi SMJ, Bordonaro GG, Ferro P, Torgersen J, Berto F. *Metals* 2017, 7(8), 291.
- (9) Razavi, S.M.J. , Ferro P. , Berto F, Torgersen J. *Theor Appl Fract Mec*. In press DOI: 10.1016/j.tafmec.2017.06.021
- (10) Leonard F., Tamas-Williams S., Prangnell P.B., Todd I., Withers P.J. , Assessment by X-ray CT of the effects of geometry and build direction on defects in titanium ALM parts, *iCT 2012 - International Conference on Industrial Computed Tomography*, Wels, Austria, 2012, pp. 85-93.
- (11) Findlay SJ and Harrison ND. *Mater Today*, 2002 Vol 5 (11), pp 18–25.

- (12) Gorelik, M. *Int J of Fatigue*, 94, pp. 168-177.
- (13) Aboulkhair, N.T., Everitt N. M., Ashcroft I., and Tuck C., *Addit. Manuf.*, 2014, 1–4, pp. 77–86.
- (14) Tamas-Williams S., Withers P.J., Todd I. and Prangnell P.B., *Sci. Rep.*, 2017, Accepted for publication.
- (15) Yadroitsev I. and Smurov I., *Phys. Procedia*, 2010, 5, pp. 551–560.
- (16) Ciurana J., Hernandez L., and Delgado J., *Int. J. Adv. Manuf. Technol.*, 2013, Vol. 68 (5–8), pp. 1103–1110
- (17) Dai D. and Gu D, *Mater. Des.*, 2014, Vol. 55, pp. 482–491.
- (18) Read N., Wang W., Essa K., Attallah M.M., *Mater. Des.*, 2015, 65, pp. 417-424.
- (19) ASTM D6773: *Standard shear test method for bulk solids using the Schulze ring shear tester*, 2016.
- (20) ASTM D7481, *Standard Test Methods for Determining Loose and Tapped Bulk Densities of Powders using a Graduated Cylinder*, 2014.
- (21) Spierings A. B., Voegtlin M., Bauer T., and Wegener K., *Prog. Addit. Manuf.*, 2016, 1 (1), pp 9–20.
- (22) Frazier, W.E. *J Mater Eng Perform*, 2014, 23 (6), pp. 1917-1928.
- (23) Tamas-Williams, S., Withers, P.J., Todd, I., Prangnell, P.B. *Metall. Mater. Trans. A* , 2016, 47 (5), pp. 1939-1946.
- (24) Tamas-Williams, S., Withers, P.J., Todd, I., Prangnell, P.B., *Scr. Mater.*, 2016, 122, pp. 72-76
- (25) Abràmoff MD, Magalhães PJ, Ram SJ. Image processing with ImageJ. *Biophotonics international* 2004;11:36-42.
- (26) K. Suzuki, I. Horiba, and N. Sugie, *Comput. Vis. Image Underst.*, 2003, 89 (1), pp. 1–23.
- (27) Thijs L, Kempen K, Kruth JP, Van Humbeeck J. Fine-structured aluminium products with controllable texture by selective laser melting of pre-alloyed AlSi10Mg powder. *Acta Materialia* 2013;61:11.
- (28) Voorhees PW. The theory of Ostwald ripening. *Journal of Statistical Physics* 1985;38:231-52.
- (29) Hirsch PB, Howie A, Nicholson R, Pashley D, Whelan MJ. Electron microscopy of thin crystals. 1965, 549 P BUTTERWORTH INC, 7300 PEARL STREET, WASHINGTON, D C 20014 1966.
- (30) ASTM. ASTM E466, Standard Metal Test Methods and Analytical Procedures. 1995.
- (31) Aerospace-series. metallic materials – test methods – constant amplitude fatigue testing. DIN EN 6072: 2010. 2010.